Asociación Argentina
de Mecánica Computacional

Mecánica Computacional Vol XXX, págs. 2233-2249 (artículo completo)
Oscar Möller, Javier W. Signorelli, Mario A. Storti (Eds.)
Rosario, Argentina, 1-4 Noviembre 2011

AEROSERVOELASTIC BEHAVIOR OF A WIND TURBINE TYPICAL SECTION WITH AN ACTIVE SMART FLEXIBLE FLAP

Nicolás G. Tripp[a,c], Sergio Preidikman[b,c], Anibal E. Mirasso[a]

[a]*IMERIS,Facultad de Ingeniería, Universidad Nacional de Cuyo, Parque General San Martín, 5501 Mendoza, Argentina, aemirasso@uncu.edu.ar*

[b]*Departamento de Estructuras, Facultad de C. E. F. y N., Universidad Nacional de Córdoba, Casilla de Correo 916, 5000 Córdoba, Argentina, spreidikman@efn.uncor.edu*

[c]*Conicet CCT Mendoza, ntripp@mendoza-conicet.gob.ar*

Keywords: Wind Energy, Smart Blades, Aeroservoelasticity, Piezoelectric transducers.

Abstract: In the past years, the consumption of energy produced by wind turbines had an exponential growth. This requirement gave momentum to the development of larger turbines with the goal of producing more energy at the same site, reducing the initial investment, and the operation and maintenance costs. In order to achieve this objective, longer, lighter, maintenance-free blades are required so that smaller loads are transferred to the other, more expensive, wind turbine components. The resulting larger flexibility, imposes new challenges to the blade and controller designs; henceforth, new concepts are being developed to add more intelligence into these systems. During the last few years, the electronics industry had invested resources into the research and development of practical applications for piezoelectric ceramic materials. The result of this effort was the development of high precision piezoelectric actuators and sensors, which achieve forces and deformations that are compatible with the ones needed for the control of aerodynamic surfaces. In this work, the aeroservoelastic behavior of a wind turbine blade typical section equipped with an active smart flap is numerically simulated. The bending and torsion stiffness of the blade are modeled by means of two springs placed at the shear center of the blade's section. The displacements associated to these two deformation modes are described by means of two discrete generalized coordinates. Structurally, the flap is modeled as a continuous beam, with fixed-free boundary conditions, and an embedded piezoelectric actuator. The bending mode of the flap is actively excited through the use of a commercially available piezoelectric actuator. The model response was compared to the data published by the actuator manufacturer. Aerodynamically, the blade-flap system is modeled assuming the hypotheses of thin airfoil theory. The aerodynamic loads are determined by replacing the vortex sheet with a two dimensional (2D) version of the non-linear, unsteady, vortex lattice method. To capture the physical aspects from the control-fluid-structure interaction, the models are combined using a strong coupling technique. The equations of motion of the system are integrated numerically and interactively in the time domain. In addition, the stability and sensitivity of the system for input perturbations are analyzed. The results show the feasibility of using this type of system in large horizontal wind energy turbines.

1 INTRODUCTION

In the past years, the consumption of energy produced by wind turbines had an exponential growth. This requirement gave momentum to the development of larger turbines with the goal of producing more energy at the same site, reducing the initial investment, and the operation and maintenance costs. In order to achieve this objective, longer, lighter, maintenance-free blades are required so that smaller loads are transferred to the other, more expensive, wind turbine components. The resulting larger flexibility, imposes new challenges to the blade and controller design, therefore new concepts are being developed to add more intelligence into these systems.

There are many former studies about this subject applied, mostly to aircraft, and to wind turbines. A good review can be seen in *Barlas and Kuik (2010).*

Embedding an active layer of piezoelectric ceramic material over a layer of a passive material allows inducing bending in the composite material, permitting a smooth control surface to be generated. This is of most importance in avoiding flow detachment.

During the last few years the electronics industry has invested resources into the research and development of practical applications for piezoelectric ceramic materials. The result of this effort was the development of high precision piezoelectric actuators, which achieve forces and deformations that are well-matched with those needed for the control of aerodynamic surfaces.

Modeling a typical section in motion exposed to unsteady aerodynamics is not an easy task. In a blade section the center of mass may have an offset from the shear center, so the resulting equations of motion are, in general, dynamically coupled. Moreover, the coupling between the heave and pitch motions results in a non-linear system. Furthermore, the unsteady flow around the airfoil gives rise to a wake that continuously modifies the pressure field around the airfoil. Finally, adding a flexible trailing edge, capable of modifying its own geometry by means of a piezoelectric effect, and doing it in such a fashion that reduces the fatigue producing loads, reveals the full complexity of the problem.

In this work, the aeroservoelastic behavior of a wind turbine blade typical section equipped with an active smart flap is numerically simulated in the time domain. The bending and torsion stiffness are modeled through two springs placed at the shear center of the typical section. The displacements associated to these deformation modes are described by means of two discrete generalized coordinates.

In the structural model, the flap is modeled as a continuous beam, with fixed-free boundary conditions, and an embedded piezoelectric actuator. The flap deflection relative to the body of the blade is described using the assumed modes method. The bending mode of the flap is actively excited by means of a commercially available piezoelectric actuator. The model response was compared to the data published by the manufacturer.

In the aerodynamic model, the blade-flap system is modeled assuming the hypotheses of thin airfoil theory; that is, as a vortex sheet attached to the airfoil mean camber line. The aerodynamic loads are determined by replacing this vortex sheet with a 2D version of the non-linear, unsteady, vortex lattice method.

To capture the physical aspects from the control-fluid-structure interaction, the models are combined using a strong coupling technique. The equations of motion of the aeroservoelastic system are integrated numerically and interactively in the time domain.

In addition, the stability and sensitivity of the system for air inflow and control signal perturbations are analyzed. The results show the feasibility of using this type of system in large horizontal wind energy turbines.

2 AEROELASTIC MODEL

2.1 Coordinate systems and nomenclature:

N: inertial (Newtonian) system.
B: body system that moves with the rigid airfoil and it is centered at the shear center.
A: flap system; same as system B but it is located at the origin of the flap.
h is the plunging displacement.
θ is the pitching displacement.
v is the flap deflection relative to the rigid airfoil.
m is the airfoil lumped mass.
I is the airfoil lumped second moment of inertia.
d1 is the offset of the center of mass from the shear center.
d2 is the offset of the flap origin from the shear center.

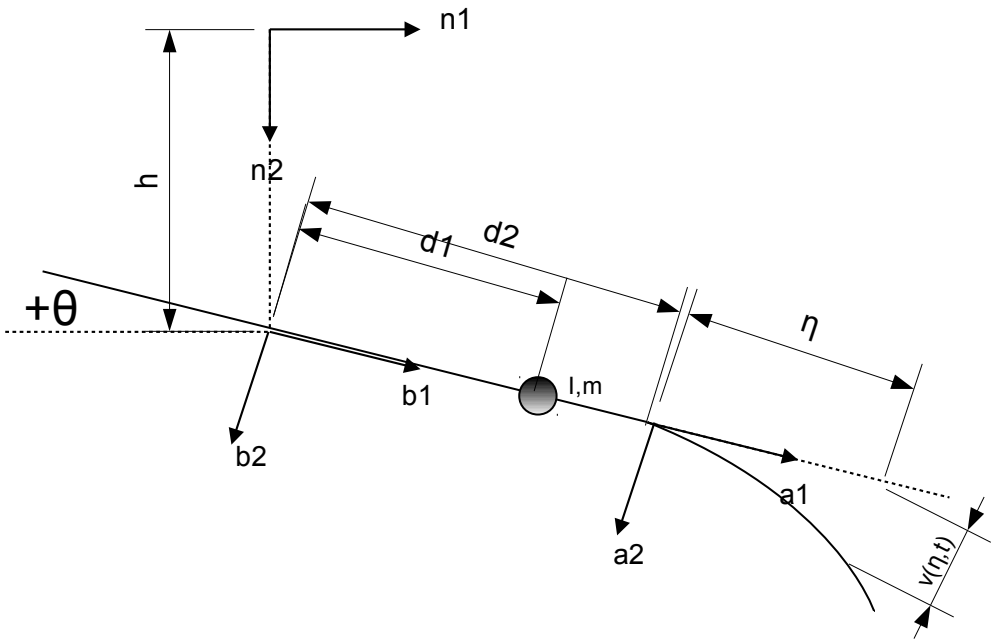

Figure 1: Model Layout

2.2 Structural model

2.2.1 Airfoil model:

The airfoil is structurally modeled as a rigid body with its mass and inertia lumped at the mass center. The mass center can be displaced from the shear center. Two discrete springs are attached at the shear center to account for bending and torsional stiffness. The spring stiffness can be determined from the frequencies typical of wind turbine blades.

$$k_h = m\omega_h^2 \quad k_\theta = I\omega_\theta^2 \tag{1}$$

where:
ω_h and ω_θ are the uncoupled plunging and pitching frequencies, respectively; and
k_h and k_θ are the plunging and pitching spring stiffness, respectively.

The position vector of the lumped mass (R) is given by:

$$R = h\,\hat{n}_2 + d_1\,\hat{b}_1 \tag{2}$$

And its velocity:

$$\dot{R} = \dot{h}\,\hat{n}_2 + \dot{\theta}\,d_1\,\hat{b}_2 \tag{3}$$

The kinetic energy is:

$$T_a = \frac{1}{2} m [\dot{R} \cdot \dot{R}] + \frac{1}{2} I\,\dot{\theta}^2 \tag{4}$$

Hence, introducing (3) in (4):

$$T_a = \frac{1}{2} m\,\dot{h}^2 + \frac{1}{2} I_a\,\dot{\theta}^2 + S_a \cos\theta\,\dot{h}\,\dot{\theta} \tag{5}$$

where:

$$\begin{aligned} S_a &= m\,d_1 \\ I_a &= I + m d_1^2 \end{aligned} \tag{6}$$

The elastic potential energy is:

$$U_a = \frac{1}{2} k_h h^2 + \frac{1}{2} k_\theta \theta^2 \tag{7}$$

2.2.2 Flap model:

The flap is modeled as a continuous beam, with fixed-free boundary conditions.

It is assumed that the mass is evenly distributed along the free span, so a constant mass per unit length (μ) is considered.

The position vector for a general point in the flap is:

$$R(\eta, t) = h\,\hat{n}_2 + d_2\,\hat{b}_1 + \eta\,\hat{a}_1 + v(\eta, t)\,\hat{a}_2 \tag{8}$$

The velocity vector is:

$$\dot{R}(\eta, t) = \dot{h}\,\hat{n}_2 + \dot{\theta}\,d_2\,\hat{b}_2 + \dot{\theta}\,\eta\,\hat{a}_2 + \dot{v}(\eta, t)\,\hat{a}_2 - \dot{\theta}\,v(\eta, t)\,\hat{a}_1 \tag{9}$$

The kinetic energy is given by:

$$T_{flap} = \frac{1}{2} \int_{flap} \dot{R} \cdot \dot{R}\,dm \tag{10}$$

Hence, replacing (8) into (9), results:

$$\begin{aligned} T_{flap} = {} & \frac{1}{2} \int_{flap} \dot{h}^2\,dm + \frac{1}{2} \int_{flap} \dot{\theta}^2 [v^2(\eta, t) + (d_2 + \eta)^2]\,dm + \ldots \\ & \ldots + \frac{1}{2} \int_{flap} [2\dot{\theta}(d_2 + \eta)\dot{v}(\eta, t) - 2\dot{h}\,\dot{\theta}\,v(\eta, t)\sin\theta + 2\,\dot{h}\dot{\theta}(d_2 + \eta)\cos\theta]\,dm + \ldots \\ & \ldots + \frac{1}{2} \int_{flap} \dot{v}^2(\eta, t)\,dm + \frac{1}{2} \int_{flap} 2\,\dot{h}\,\dot{v}(\eta, t)\cos\theta\,dm \end{aligned} \tag{11}$$

Defining the following identities:

$$
\begin{aligned}
&m_{flap} = \int_{flap} dm \\
&I_{flap} = \bar{I}_{flap} + \bar{\bar{I}}_{flap} \\
&\bar{I}_{flap} = \int_{flap} (d_2 + \eta)^2 \, dm \\
&\bar{\bar{I}}_{flap} = \int_{flap} v^2(\eta, t) \, dm \\
&S_{flap} = \bar{S}_{flap} \cos\theta - \bar{\bar{S}}_{flap} \sin\theta \\
&\bar{S}_{flap} = \int_{flap} (d_2 + \eta) \, dm \\
&\bar{\bar{S}}_{flap} = \int_{flap} v(\eta, t) \, dm \\
&\tilde{S}_{flap} = \int_{flap} (d_2 + \eta) \dot{v}(\eta, t) \, dm
\end{aligned}
\tag{12}
$$

The flap deflection, relative to the body of the blade, is described using the assumed modes method, where the displacement field can be described by the superposition of an infinite number of shape functions weighted by coefficients that are functions of time, as follows:

$$
\begin{aligned}
&v(\eta, t) = \sum \varphi_i(\eta) q_i(t) \\
&\dot{v}(\eta, t) = \sum \varphi_i(\eta) \dot{q}_i(t) \\
&v^2(\eta, t) = \sum_i \sum_j \varphi_i(\eta) \varphi_j(\eta) q_i(t) q_j(t) \\
&\dot{v}^2(\eta, t) = \sum_i \sum_j \varphi_i(\eta) \varphi_j(\eta) \dot{q}_i(t) \dot{q}_j(t)
\end{aligned}
\tag{13}
$$

Replacing (12) into (11):

$$
\begin{aligned}
&I_{flap} = \bar{I}_{flap} + \sum \sum \bar{\bar{I}}_{flap(ij)} q_i(t) q_j(t) \\
&\bar{\bar{I}}_{flap(ij)} = \int_{flap} \varphi_i(\eta) \varphi_j(\eta) \, dm \\
&S_{flap} = \bar{S}_{flap} \cos\theta - \sin\theta \sum \bar{\bar{S}}_{flap(i)} q_i(t) \\
&\bar{\bar{S}}_{flap(i)} = \int_{flap} \varphi_i(\eta) \, dm \\
&\tilde{S}_{flap(i)} = \int_{flap} (d_2 + \eta) \varphi_i(\eta) \, dm
\end{aligned}
\tag{14}
$$

Finally, replacing (11) and (13) into (10) results:

$$
\begin{aligned}
&T_{flap} = \frac{1}{2} m_{flap} \dot{h}^2 + \frac{1}{2} [\bar{I}_{flap} + \sum \sum \bar{\bar{I}}_{flap(ij)} q_i(t) q_j(t)] \dot{\theta}^2 + \ldots \\
&\ldots + \frac{1}{2} [\sum \sum \bar{\bar{I}}_{flap(ij)} \dot{q}_i(t) \dot{q}_j(t)] + \ldots \\
&\ldots + \dot{h} \dot{\theta} [\bar{S}_{flap} \cos\theta - \sin\theta \sum \bar{\bar{S}}_{flap(i)} q_i(t)] + \dot{h} \cos\theta \sum \bar{\bar{S}}_{flap(i)} \dot{q}_i(t) + \dot{\theta} \sum \tilde{S}_{flap(i)} \dot{q}_i(t)
\end{aligned}
\tag{15}
$$

2.2.3 Piezoelectric material model:

In this work, following *Preidikman et al (2006),* a simple linear model is used. It is assumed that the piezoelectric layer is polarized in its thickness direction. The free deformation (Λ) is given by:

$$\Lambda = \frac{d}{t_c} V \tag{16}$$

where:
d is a material constant that defines the piezoelectric strength;
tc is the thickness of the layer; and
V is the control voltage.

The properties of the piezoelectric and support layers were taken from a data sheet of a commercially available actuator *(see THUNDER datasheet)*.

The actuator is a composite material where the bottom layer is made from steel and the upper layer is made from a piezoelectric PZT ceramic. The beam has fixed-free boundary conditions and its bending deflection is approximated by equation (13).

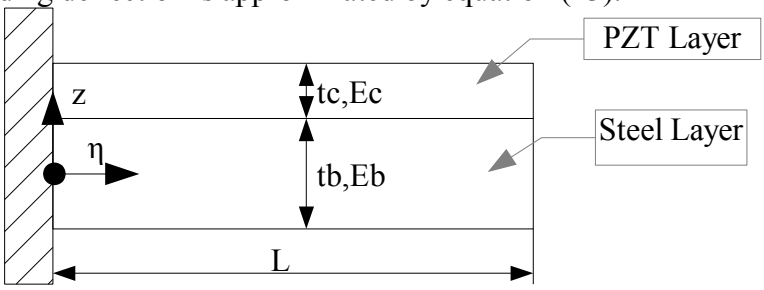

Figure 2: Flap Layout

The strain energy of the flap is given by,

$$U_{flap} = \frac{1}{2}\int \sigma \varepsilon \, dvol = \frac{1}{2}\int\int E \varepsilon^2 \, dA \, d\eta \tag{17}$$

Euler-Bernoulli slender beam hypotheses are considered and only the strain from pure bending is included.

$$\varepsilon = -(z - z_e)\frac{\partial^2}{\partial \eta^2} v + \Lambda = -(z - z_e) v'' + \Lambda$$
$$z_e = \frac{E_c t_c (t_b + \frac{t_c}{2}) + E_b t_b (\frac{t_b}{2})}{E_c t_c + E_b t_b} \tag{18}$$

Combining (13) and (19) results:

$$\varepsilon = -(z - z_e)\left[\sum \varphi_i''(\eta) q_i(t)\right] + \Lambda \tag{19}$$

and:

$$\varepsilon^2 = (z - z_e)^2 \left[\sum\sum \varphi_i''(\eta)\varphi_j''(\eta) q_i(t) q_j(t)\right] - 2(z - z_e)\sum \varphi_i''(\eta) q_i(t)\Lambda + \Lambda^2 \tag{20}$$

The integral over the thickness is evaluated in two separate regions, the steel layer and the PZT layer, which results in:

$$
\begin{aligned}
&U_{flap}=\frac{1}{2}\sum\sum q_i(t)q_j(t)\bar{K}_{ij}+\frac{1}{2}\sum\sum q_i(t)q_j(t)\bar{\bar{K}}_{ij}+\ldots\\
&\ldots-\sum q_i(t)Fe_i+E_c\,L\,b\,t_c\Lambda^2\\
&\bar{K}_{ij}=\int_0^L \varphi_i''(\eta)\varphi_j''(\eta)E_b I_b d\,\eta\\
&I_B=\int_{A_b}(z-z_e)^2 dA\\
&\bar{\bar{K}}_{ij}=\int_0^L \varphi_i''(\eta)\varphi_j''(\eta)E_c I_c d\,\eta\\
&I_c=\int_{A_c}(z-z_e)^2 dA\\
&Fe_i=\int_0^L \varphi_i''(\eta)E_c S_c\Lambda\, d\,\eta\\
&S_c=\int_{t_b}^{t_b+t_c}(z-z_e)dA
\end{aligned}
\tag{21}
$$

2.3 Unsteady Aerodynamics:

A thorough explanation of this model can be found in *Katz & Plotkin (1991).*

The airfoil is modeled assuming the hypotheses of thin airfoil theory; that is, as a vortex sheet attached to the airfoil mean camber line.

It is assumed that the flow surrounding the airfoil and its wake is inviscid, irrotational and incompressible, hence there is a velocity potential that fulfills the Laplace equation, which describes its spatial distribution:

$$\nabla^2\Phi=0 \tag{22}$$

In order to have a unique solution, three additional conditions must also be satisfied:

1. The flow is tangent to the airfoil boundaries (zero normal flow):

$$
\begin{aligned}
&(\nabla\Phi+\vec{v})\cdot\vec{n}=0\\
&\vec{v}=-[\vec{v}_\infty+\vec{v}_{body}]
\end{aligned}
\tag{23}
$$

2. The flow disturbances vanish far from the body:

$$\lim_{d\to\infty}\nabla\Phi=0 \tag{24}$$

3. The total circulation is constant for all t:

$$\frac{d}{dt}\Gamma=0 \tag{25}$$

The second condition is fulfilled by selecting the lumped vortex solution, where the airfoil vortex sheet is discretized with panels as the one shown in figure 3.

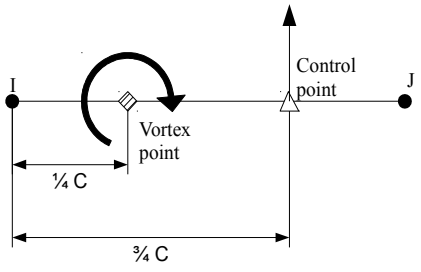

Figure 3: Panel element

The vorticity is lumped into a single vortex at the panel quarter-chord. The induced velocity is evaluated at the control point located at the panel three-quarter-chord. The velocity induced by a single vortex can be written in the following matrix form:

$$\begin{aligned}
&\nabla\Phi=\begin{pmatrix}u\\w\end{pmatrix}=\frac{\Gamma}{2\pi r^2}\begin{pmatrix}0&1\\-1&0\end{pmatrix}\begin{pmatrix}x_c-x_v\\z_c-z_v\end{pmatrix}=\vec{a_{cv}}\,\Gamma\\
&\vec{a_{cv}}=\frac{1}{2\pi r^2}\begin{pmatrix}0&1\\-1&0\end{pmatrix}\begin{pmatrix}x_c-x_v\\z_c-z_v\end{pmatrix}\\
&r^2=(x_c-x_v)^2+(z_c-z_v)^2
\end{aligned}\tag{26}$$

where (x_c,z_c) are the coordinates of the control point and (x_v,z_v) are the coordinates of the concentrated vortex.

It is further assumed that there is no flow separation (no stall) and the boundary layer thickness is sufficiently small so its influence on the airfoil geometry can be neglected.

Now the velocity potential can be divided into an airfoil potential and a wake potential.

$$\Phi=\Phi_{airfoil}+\Phi_{wake}\tag{27}$$

Replacing (27) into (23) results:

$$\begin{aligned}
&(\nabla\Phi_{airfoil}+\nabla\Phi_{wake}-\vec{v_\infty}-\vec{v_{body}})\cdot\vec{n}=0\\
&\rightarrow\nabla\Phi_{airfoil}\cdot\vec{n}=-(\nabla\Phi_{wake}+\vec{v_\infty}+\vec{v_{body}})\cdot\vec{n}
\end{aligned}\tag{28}$$

And taking into account that the total potential at any point is the sum of all the vortex contributions:

$$\nabla\Phi_{airfoil(i)}=\sum_j\vec{a}_{ij}\Gamma_{airfoil(i)}\tag{29}$$

From the third boundary condition, the vorticity in the wake has to be constant in time, therefore its value is known at each time step.

Replacing (29) into (28) and expressing the result in matrix form yields:

$$\begin{aligned}
&A\,\Gamma_{airfoil}=-(\nabla\Phi_{wake}+\vec{v_\infty}+\vec{v_{body}})\cdot\vec{n}=\vec{RHS}\\
&\vec{RHS}=-(\nabla\Phi_{wake}+\vec{v_\infty}+\vec{v_{body}})\cdot\vec{n}
\end{aligned}\tag{30}$$

where A is the matrix of aerodynamic influence coefficients:

$$A_{(ij)}=(\sum_j\vec{a}_{ij})\cdot\vec{n}_i\tag{31}$$

When the airfoil is accelerating from rest, a starting vortex is shed from its trailing edge to cancel the airfoil circulation, so an additional vortex is present at the flow field. This requires the introduction of an additional equation.

$$\begin{aligned}
&\Gamma(t)-\Gamma(t-\Delta t)+\Gamma_w=0\\
&\Gamma(t)=\sum\Gamma_{airfoil(i)}
\end{aligned}\tag{32}$$

At each time step, a linear system of algebraic equations is solved in order to evaluate the circulation around the airfoil.

Having defined the system completely, the induced velocities at the airfoil and its wake are then calculated. Having this information, the airfoil tangential velocities and pressures are determined using the unsteady version of the Bernoulli equation. This is needed due to fact that the equations are solved in a local coordinate system and the Bernoulli equation is valid on an inertial coordinate system.

$$\Delta p_j = \rho\left(U_\infty \frac{\Gamma_j}{\Delta l_j} + \frac{\partial}{\partial t}\sum_1^j \Gamma_k\right) \tag{33}$$

Once the panel pressures are calculated the wake is reconfigured using the total velocity field; then, time is incremented, and all the previous steps are repeated.

2.3.1 Generalized forces

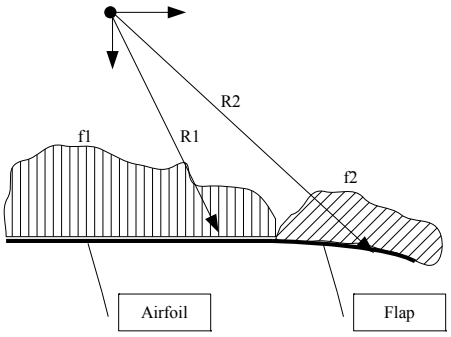

Figure 4: Pressure loads

The virtual work done by the pressure field acting on the typical section is given by:

$$\delta \bar{W} = \int_{airfoil} \vec{f}_1(\xi, t)\cdot\delta R_1(\xi, t)\, d\xi + \int_{flap} \vec{f}_2(\eta, t)\cdot\delta R_2(\eta, t)\, d\eta = \delta \bar{W}_1 + \delta \bar{W}_2 \tag{34}$$

where:

$$\vec{f}_1(\xi,t)=-f_1(\xi,t)\hat{b}_2$$
$$R_1=h\hat{n}_2+\xi\hat{b}_1$$
$$\delta R_1=\delta h\,\hat{n}_2+\xi\,\delta\hat{b}_1$$
$$\delta\hat{b}_1=\delta\theta\,\hat{b}_3\times\hat{b}_1=\delta\theta\,\hat{b}_2$$
$$\delta R_1=\delta h\,\hat{n}_2+\xi\,\delta\theta\,\hat{b}_2$$
$$\vec{f}_1(\xi,t)\cdot\delta R_1=-f_1\cos\theta\,\delta h-f_1\xi\,\delta\theta$$
$$\vec{f}_2(\eta,t)=-f_2(\eta,t)(\sin\beta\hat{b}_1-\cos\beta\hat{b}_2) \tag{35}$$
$$R_2=h\hat{n}_2+(d_2+\eta)\hat{b}_1+v\hat{b}_2$$
$$\delta R_2=\delta h\,\hat{n}_2+(d_2+\eta)\,\delta\hat{b}_1+\delta v\,\hat{b}_2+v\,\delta\hat{b}_2$$
$$\delta\hat{b}_1=\delta\theta\,\hat{b}_3\times\hat{b}_1=\delta\theta\,\hat{b}_2$$
$$\delta\hat{b}_2=\delta\theta\,\hat{b}_3\times\hat{b}_2=-\delta\theta\,\hat{b}_1$$
$$\delta R_2=\delta h\,\hat{n}_2+((d_2+\eta)\delta\theta+\delta v)\hat{b}_2-v\,\delta\theta\,\hat{b}_1$$
$$\vec{f}_2(\eta,t)\cdot\delta R_2=-f_2\cos(\theta+\beta)\,\delta h-f_2[\sin\beta\,v+\cos\beta(d_2+\eta)]\,\delta\theta-f_2\cos\beta\,\delta v$$

and recalling (13):

$$\delta v=\sum_i\varphi_i(\eta)\,\delta q_i(t) \tag{36}$$

Replacing (34) into (35) and using (36) yields:

$$\begin{aligned}
&\delta\bar{W}=\delta\bar{W}_1+\delta\bar{W}_2=Q_h\cdot\delta h+Q_\theta\cdot\delta\theta+\sum_i Q_{q(i)}\cdot\delta q_i\\
&Q_h=-\int_{airfoil}f_1\cos\theta\,d\xi-\int_{flap}f_2\cos(\theta+\beta)\,d\eta\\
&Q_\theta=-\int_{airfoil}f_1\xi\,d\xi-\int_{flap}f_2[\sin\beta\sum_i\varphi_i(\eta)q_i(t)+\cos\beta(d_2+\eta)]\,d\eta\\
&Q_{q(i)}=-\int_{flap}f_2\cos\beta\sum_i\varphi_i(\eta)\,d\eta
\end{aligned} \tag{37}$$

2.4 Combining the models - equations of motion

The expressions for the kinetic and potential energies, along with the expression for the generalized forces are now replaced into Lagrange's equations leading to,

$$\frac{d}{dt}\frac{\partial}{\partial \dot{q}_i}(T_a+T_{flap})-\frac{\partial}{\partial q_i}(T_a+T_{flap})+\frac{\partial}{\partial q_i}(U_a+U_{flap})=Q_i \tag{38}$$

The resulting differential equations of motion, in matrix form, are:

$$\begin{bmatrix} m_{hh} & m_{h\theta} & m_{hq_1} & m_{hq_i} \\ m_{\theta h} & m_{\theta\theta} & m_{\theta q_1} & m_{\theta q_i} \\ m_{q_1 h} & m_{q_1\theta} & m_{q_1 q_1} & m_{q_1 q_i} \\ m_{q_i h} & m_{q_i\theta} & m_{q_i q_1} & m_{q_i q_i} \end{bmatrix} \cdot \begin{Bmatrix} \ddot{h} \\ \ddot{\theta} \\ \ddot{q}_1 \\ \ddot{q}_i \end{Bmatrix} + \begin{bmatrix} K_h & 0 & 0 & 0 \\ 0 & K_\theta & 0 & 0 \\ 0 & 0 & (\bar{K}_{11}+\bar{\bar{K}}_{11}) & (\bar{K}_{1i}+\bar{\bar{K}}_{1i}) \\ 0 & 0 & (\bar{K}_{iI}+\bar{\bar{K}}_{iI}) & (\bar{K}_{ii}+\bar{\bar{K}}_{ii}) \end{bmatrix} \cdot \begin{Bmatrix} h \\ \theta \\ q_1 \\ q_i \end{Bmatrix} = \begin{Bmatrix} Q_h \\ Q_\theta \\ Q_{q_1} \\ Q_{q_i} \end{Bmatrix} - \begin{Bmatrix} B_h \\ B_\theta \\ B_{q_1} \\ B_{q_i} \end{Bmatrix}$$

$$m_{hh}=m+m_{flap}$$
$$m_{h\theta}=(S_a+\bar{S}_{flap})\cos\theta-\sum_i \bar{\bar{S}}_{flap(i)}$$
$$m_{hqi}=\cos\theta\,\bar{\bar{S}}_{flap(i)}$$
$$m_{\theta\theta}=I_a+\bar{I}_{flap}+\sum\sum \bar{\bar{I}}_{flap}q_i(t)q_j(t)$$
$$m_{\theta q_i}=\tilde{S}_{flap(i)}$$
$$m_{q_i q_j}=\bar{\bar{I}}_{flap(ij)}$$
$$B_h=-\dot{\theta}^2[(S_a+\bar{S}_{flap})\sin\theta+(\sum \bar{\bar{S}}_{flap(i)}q_i(t))\cos\theta]-2\dot{\theta}\sin\theta\sum \bar{\bar{S}}_{flap(i)}\dot{q}_i$$
$$B_\theta=[\sum\sum \bar{\bar{I}}_{flap(ij)}(\dot{q}_i q_j+q_i\dot{q}_j)]\dot{\theta}$$
$$B_{qi}=-\dot{\theta}^2\sum \bar{\bar{I}}_{flap(ij)}q_j(t)$$

(39)

This system is integrated in the time domain using a step-by-step Euler algorithm.

For the test cases analyzed in this work the angle β is assumed to be zero. Therefore the aerodynamic loads are normal to the airfoil chord. For the flap tip displacement resulting from the test cases (5 mm), the error generated from this assumption is minimum.

3 RESULTS

3.1 Validation

In order to validate the predicted results, the aerodynamic model is first tested against the steady state thin airfoil theory. The wind inflow is set at 10 m/s and 10º of angle of attack. From thin airfoil theory hypotheses, the force and aerodynamic moment, measured at the quarter chord, for a flat plate are:

$$
\begin{aligned}
&L = P_{dyn}\, c\, C_l = 67{,}167\, N \\
&P_{dyn} = \frac{1}{2}\rho\, V_\infty^2 = 61{,}25\, P_a \\
&C_l = 2\pi\alpha = 2\pi\left(\frac{10^o}{180^o}\pi\right) = 1{,}0966 \\
&M_{c/4} = Pdyn\, c^2\, C_{m_{c/4}} = 0\, Nm \\
&C_{m_{c/4}} = 0
\end{aligned}
\tag{40}
$$

To select the number of panels required for the aeroservoelastic simulations three runs were performed and the results are shown in Table 1.

Nº of panels	L (N)
10	63,95
50	64,94
100	65,76

Table 1: Model convergence on number of panels.

Results after 4 seconds (200 steps of 20 msec) and using 100 panels:

$L = 65{,}76\, N$

$M_{c/4} = 0{,}001651\, Nm$

The model results and the wake geometry are shown in figure 5.

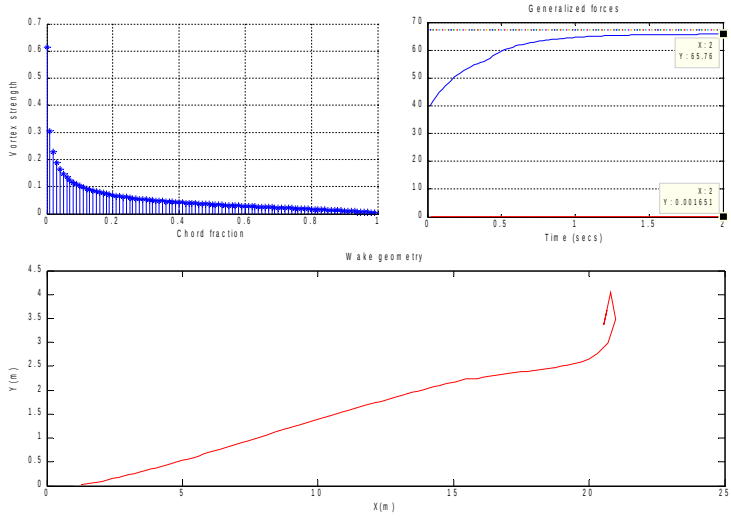

Figure 5: Aerodynamic model test results.

To validate the algorithm used to take into account the interaction between the models, the work of *Johansen (1999)* is used as reference. In the reference the typical section is modeled as a rigid airfoil and the aerodynamic is modeled using CFD.

One dimensional model tests are carried out and compared to *Johansen (1999)* results. In figure 6 pitch angle oscillations and plunge displacement from the reference data is shown. In figures 7 and 8 the displacement, forces and wake geometry from the model are presented.

In this test the shear center is located at the quarter-chord and the system properties are the following: m=64,65kg/m, I=29,09 kg.m, Vinf=28,15m/s, Rho=1,293kg/m3, c=1m, d1=0,15.

For the plunge test, a 0,1 initial displacement is applied, while for the pitching test, a 6º initial pitch is used.

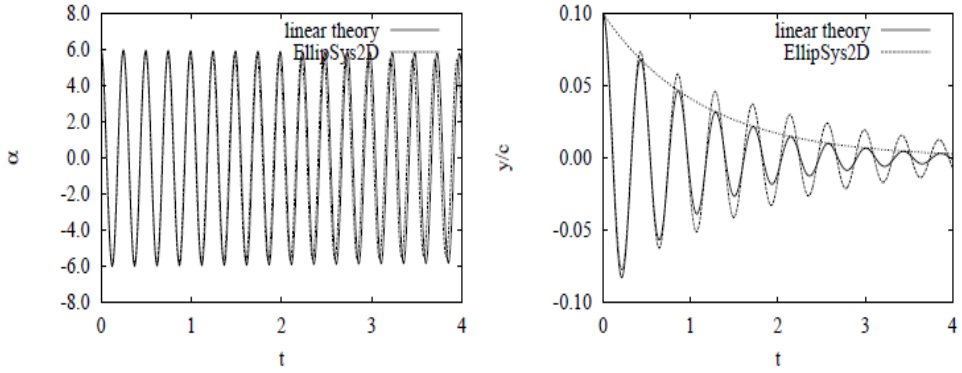

Figure 6: Single degree of freedom test from reference.

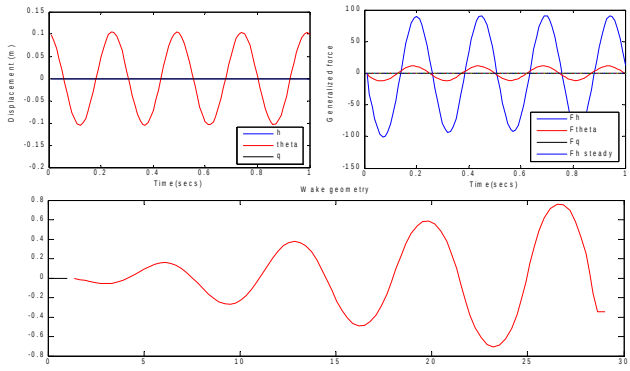

Figure 7: Single (pitch) degree of freedom test results from present model.

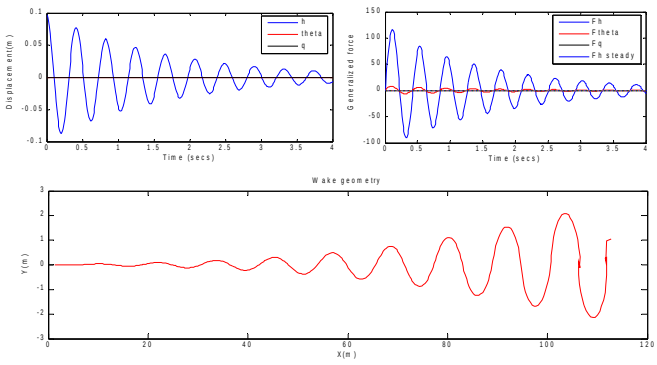

Figure 8: Single (plunge) degree of freedom test results from present model.

Damping calculation: one of the objectives of adding a control surface to this system is to reduce vibrations. So it is reasonable to determine the critical damping ratio for the reference case as well as the other cases.
Damping can be measured by means of the logarithmic decrement and then the critical damping ratio can be estimated from this value. The formulas for each value are defined next:

$$\delta = \frac{1}{m} \ln\left(\frac{h_0}{h_{t+m\Delta T}}\right)$$
$$\varepsilon = \frac{\delta}{2\pi} 100 \qquad \textbf{(41)}$$

where:
δ is the logarithmic decrement.
m is the number of cycles between measurements.
hi is the displacement at time i.
ε is the critical damping ratio in %.

For the reference case (plunging):

For only one cycle: $\delta = \ln\left(\frac{h_0}{h_{t+\Delta T}}\right) = \ln\left(\frac{0,1}{0,07724}\right) = 0,25825$
$\varepsilon = 4,11$

For 9 cycles: $\delta = \frac{1}{9} \ln\left(\frac{h_0}{h_{t+9\Delta T}}\right) = \frac{1}{9} \ln\left(\frac{0,1}{0,01042}\right) = 0,25127$
$\varepsilon = 3,999$

For the reference case (pitching):

For only one cycle: $\delta = \ln\left(\frac{\theta_0}{\theta_{t+\Delta T}}\right) = \ln\left(\frac{0,10472}{0,1051}\right) = -3,6-3$
$\varepsilon = -0,06$

For 8 cycles: $\delta = \frac{1}{8} \ln\left(\frac{\theta_0}{\theta_{t+8\Delta T}}\right) = \frac{1}{8} \ln\left(\frac{0,1047}{0,08897}\right) = 0,02035$
$\varepsilon = 0,324$

3.2 Plunging motion and deformable flap coupling (passive)

In this test only the pitching motion is constrained. The same properties as in the reference case are used, so that the effect of having a flap is emphasized.

Since the flap has greater stiffness than the plunge spring, the time step is reduced to 1.5msecs.

The results of these simulations are shown in figure 9.

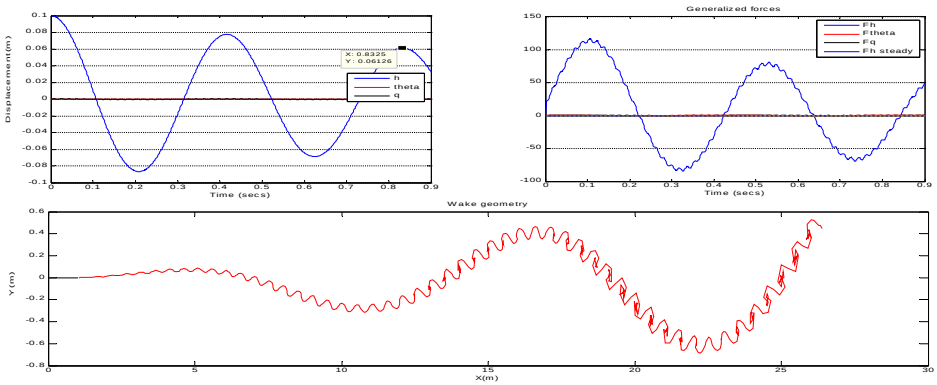

Figure 9: Plunge and passive flap coupling results.

The flap vibration can be perceived in the wake shed into the flow.

The resulting damping values are:

$$\delta = \frac{1}{2}\ln\left(\frac{0{,}1}{0{,}06126}\right) = 0{,}245$$

$$\varepsilon = 3{,}899$$

3.3 Plunging motion and deformable flap coupling (active)

Now, a simple feedback control law is added to the flap.

$$V = Vmax \cdot \dot{h} \tag{42}$$

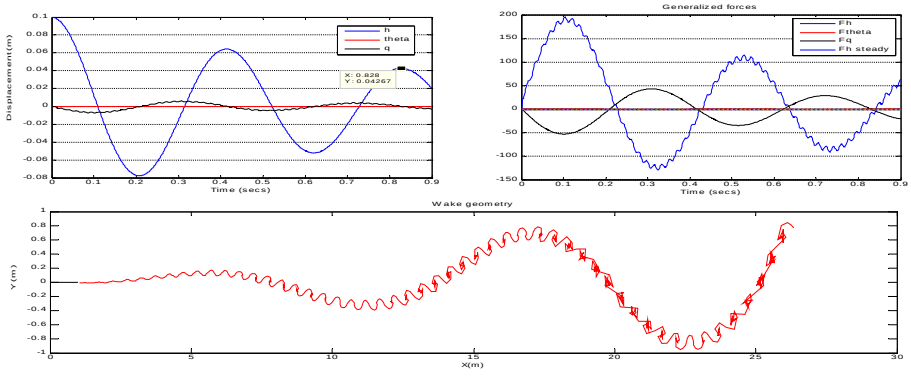

Figure 10: Plunge and active flap coupling results.

The resulting damping values are:

$$\delta = \frac{1}{2}\ln\left(\frac{0{,}1}{0{,}04268}\right) = 0{,}4257$$

$$\varepsilon = 6{,}77$$

3.4 Pitching motion and deformable flap coupling (passive)

In this test the plunging motion is inhibited. The same properties as in the reference case are used, so that the flap effects can be highlighted.

Since the flap has greater stiffness than the pitch spring, the time step is reduced to 1.5msecs.

The results are shown in figure 11

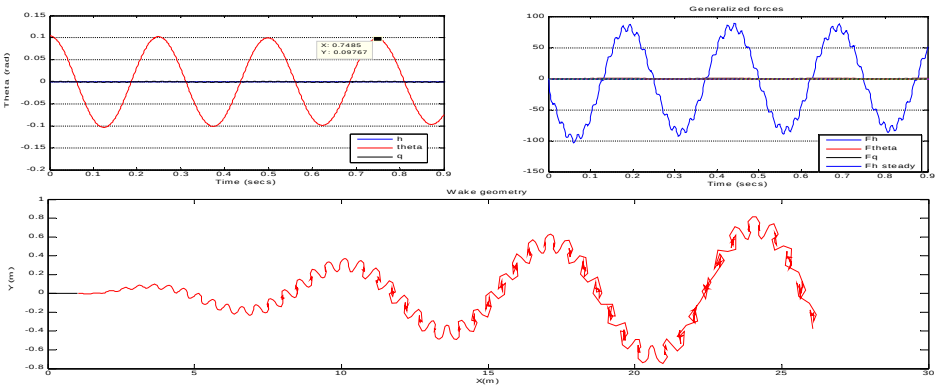

Figure 11: Pitch and passive flap coupling results.

The flap vibration can be seen in the wake shed into the flow.

The resulting damping values are:

$$\delta = \frac{1}{3}\ln\left(\frac{0{,}1047}{0{,}09767}\right) = 0{,}023168$$

$$\varepsilon = 0{,}369$$

3.5 Pitching motion and deformable flap coupling (active)

In this case, the same feedback control law is added to the flap but using the pitching velocity instead.

$$V = Vmax \cdot \dot{\theta} \tag{43}$$

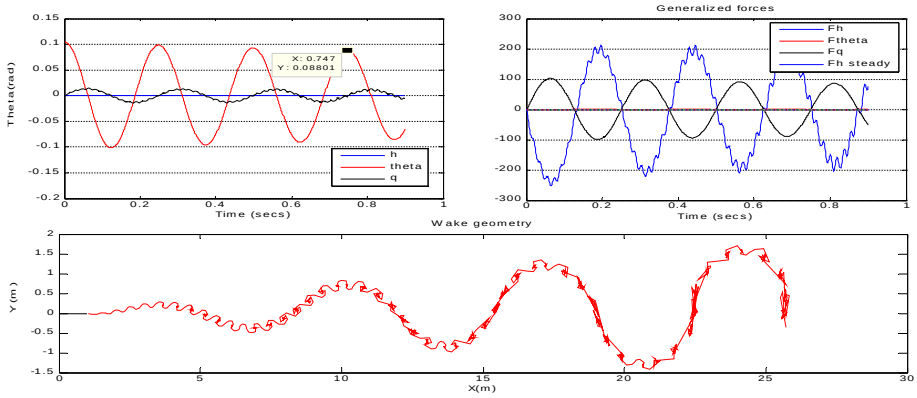

Figure 12: Pitch and active flap coupling results.

The resulting damping values are:

$$\delta = \frac{1}{2}\ln\left(\frac{0{,}1047}{0{,}08801}\right) = 0{,}05788$$

$$\varepsilon = 0{,}921$$

4 CONCLUSIONS

In this work, the aeroservoelastic behavior of a wind turbine blade typical section equipped with an active smart flexible flap is numerically simulated. The unsteady aerodynamic is modeled by means of thin airfoil theory and the resulting equations are discretized using the unsteady version of the vortex lattice method. The geometry of the wake is found, iteratively, using a time-stepping technique. The flap is modeled as a multilayered flexible beam with some layers having piezoelectric properties. This allows a control law to be applied evenly over the entire flap. The bending and torsion stiffness are modeled through two linear springs placed at the shear center of the typical section. In this model, the structural damping is not taken into account. The equations of motion of the aeroservoelastic system are integrated numerically and interactively in the time domain using a step-by-step Euler algorithm.

The aerodynamic model is validated against thin airfoil theory for a flat plate in steady state condition. The aeroelastic model predictions of a rigid typical section are compared to available results from other authors.

The addition of a passive flexible flap with a chord of 10% of the airfoil chord does not seem to introduce considerable changes in the uncoupled (plunge or pitch) system damping behavior. The results show that adding a simple plunge velocity feedback control law in the piezoelectric layers can increase bending damping up to 73%. Greater effects are seen for the pitching motion by a simple pitch velocity feedback control law. In the latest case a 150% increase in damping is observed, against the critical damping of 0,39% measured in the passive case. From the results, it is also seen that the dynamics of the flap introduces high frequency vibration into the system that should be taken into account when analyzing a more complex feedback rule.

These results show the feasibility of using this type of system in large horizontal axis wind turbines.

REFERENCES

Barlas T. and Van Kuik G. Review of state of the art in smart rotor control research for wind turbines. *Progress in Aerospace Sciences*,46:1-27,2010.

Face International Corporation, *THUNDER® TH-6R Data Sheet.* http://216.71.30.251/Face%20International/6r-ds.pdf

Johansen J. Unsteady Airfoil Flows with Application to Aeroelastic Stability. *Risø Laboratory*, Risø–R–1116(EN).

Katz J. and Plotkin A. *LOW SPEED AERODYNAMICS – From wing theory to panel methods.* McGraw-Hill, 1991.

Preidikman S., Massa J. and Bandi M. Accionamiento mediante actuadores piezoeléctricos de alas flexibles para micro-vehículos aéreos súper maniobrables inspirados en la biología. *Mecánica computacional* , 25:2359-2381,2006.